ACS OMEGA

http://pubs.acs.org/journal/acsodf

Article

Characterizing the Dynamic Disassembly/Reassembly Mechanisms of Encapsulin Protein Nanocages

India Boyton, Sophia C. Goodchild, Dennis Diaz, Aaron Elbourne, Lyndsey E. Collins-Praino, and Andrew Care*

Cite This: *ACS Omega* 2022, 7, 823−836

Read Online

ACCESS | Metrics & More | Article Recommendations | Supporting Information

ABSTRACT: Encapsulins, self-assembling icosahedral protein nanocages derived from prokaryotes, represent a versatile set of tools for nanobiotechnology. However, a comprehensive understanding of the mechanisms underlying encapsulin self-assembly, disassembly, and reassembly is lacking. Here, we characterize the disassembly/reassembly properties of three encapsulin nanocages that possess different structural architectures: $T = 1$ (24 nm), $T = 3$ (32 nm), and $T = 4$ (42 nm). Using spectroscopic techniques and electron microscopy, encapsulin architectures were found to exhibit varying sensitivities to the denaturant guanidine hydrochloride (GuHCl), extreme pH, and elevated temperature. While all three encapsulins showed the capacity to reassemble following GuHCl-induced disassembly (within 75 min), only the smallest $T = 1$ nanocage reassembled after disassembly in basic pH (within 15 min). Furthermore, atomic force microscopy revealed that all encapsulins showed a significant loss of structural integrity after undergoing sequential disassembly/reassembly steps. These findings provide insights into encapsulins' disassembly/reassembly dynamics, thus informing their future design, modification, and application.

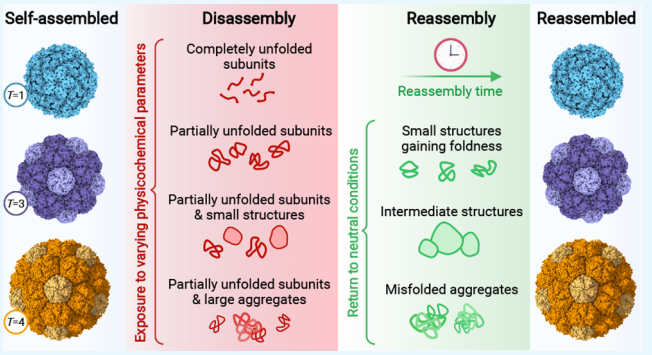

INTRODUCTION

Protein nanocages [e.g., virus-like particles (VLPs), ferritins, heat-shock proteins] self-assemble from multiple protein subunits into highly organized macromolecular structures, which exhibit well-defined inner cavities, outer surfaces, and interfaces between subunits. Their capacity to encapsulate cargo, coupled with the ability to genetically and/or chemically modify their structures, has enabled protein nanocages to be custom-engineered for a multitude of applications, including biocatalysis, materials synthesis, sensing, vaccines, and drug delivery.[1,2]

Encapsulins are an emerging class of protein nanocages found inside many archaea and bacteria. They self-assemble from identical protein subunits into hollow icosahedral nanocages that structurally resemble the major capsid protein gp5 of the HK97 virus.[3,4] Based on their triangulation number (T), all encapsulins exhibit one of the following three symmetrical icosahedral architectures: $T = 1$ (24 nm, 60-mer, 12 pentameric units), $T = 3$ (32 nm, 180-mer, 12 pentameric and 20 hexameric units), and $T = 4$ (42 nm, 240-mer, 12 pentameric and 30 hexameric units).[5−8] In nature, encapsulins house cargo enzymes that mediate oxidative stress resistance, iron storage, anaerobic ammonium oxidation, or sulfur metabolism.[9−12] Uniquely, encapsulins selectively self-assemble around cargo enzymes tagged with a small encapsulation signal peptide (ESig), packaging them.[5] This mechanism has been adapted to load foreign cargo into encapsulins, reprograming their functionality for different practical applications.[13]

Encapsulin subunits autonomously assemble, with extraordinary fidelity, into macromolecular nanocages. Such self-assembly is driven not only by folding of the individual polypeptide chains but also by dynamic noncovalent interactions between the different polypeptide chains both within subunits and at the interfaces between subunits in the assembled supramolecular structure.[14] Unraveling the self-assembly mechanisms of protein nanocages is complicated, especially if they exhibit highly symmetric homo-oligomeric structures, such as encapsulins.[15] Nevertheless, multiple analytical techniques now allow the molecular mechanisms underlying protein nanocage assembly (e.g., protein folding) to be characterized and subsequently exploited.

Received: October 1, 2021
Accepted: November 19, 2021
Published: December 20, 2021

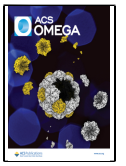

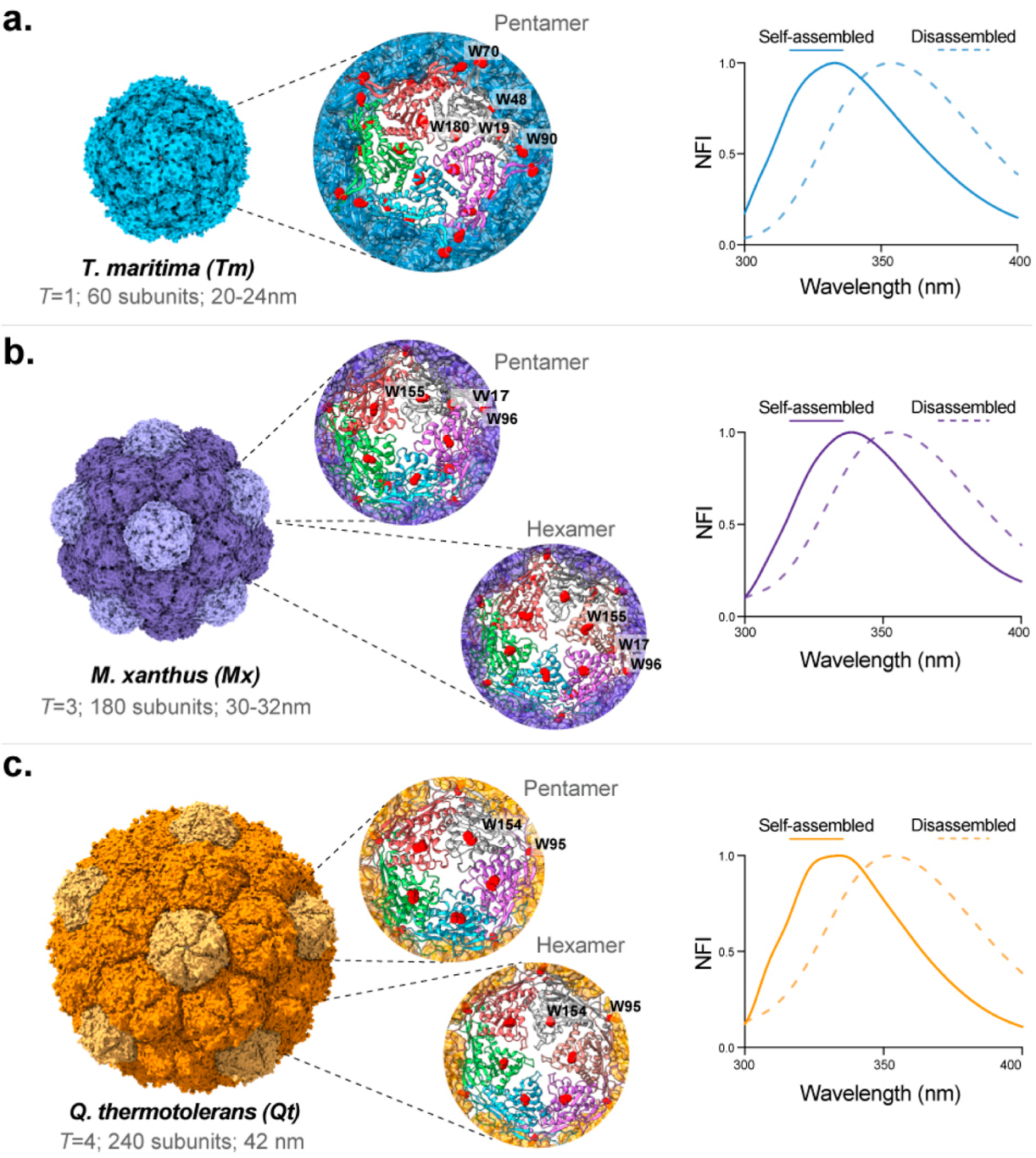

Figure 1. Monitoring encapsulin nanocage assembly states via ITF spectroscopy. Schematic diagram showing the assembled architectures of (a) *Tm-Enc* (PDB: 3DKT), (b) *Mx-Enc* (PDB: 4PT2), and (c) *Qt-Enc* (PDB: 6NJ8). For each structure, the pentameric and hexameric units are shown in light and saturated colors, respectively. Within the expanded pentameric or hexameric units, the tryptophan (W) residues belonging to individual subunits are highlighted in red: *Tm*: W19, W48, W70, W90, and W180; *Mx*: W17, W96, and W155; and *Qt*: W95 and W154. Molecular graphics were created using UCSF ChimeraX.[30] Using ITF spectroscopy, a shift in emission discriminated between the maximum emission wavelength of buried Trp in the "assembled" form: ~334 nm for (a) *Tm-Enc* and (c) *Qt-Enc*, or ~338 for (b) *Mx-Enc*, and solvent-exposed Trp in the "disassembled" form (~354 nm) upon addition of 7 M GuHCl. Normalized fluorescence intensity (NFI) was achieved by making the maximum Trp emission wavelength (nm) = 1.

For instance, the disassembly/reassembly of protein nanocages belonging to the ferritin family have been studied via a combination of intrinsic tryptophan fluorescence (ITF), circular dichroism (CD), and UV/vis spectroscopy and synchrotron small-angle X-ray scattering measurements to assess the protein conformation;[16−19] transmission electron microscopy (TEM) and dynamic light scattering (DLS) to evaluate the structural integrity, shape, and size distribution; and laser light scattering to monitor the assembly kinetics.[20] One study revealed that ferritin disassembles at an extremely acidic pH 1.5 and then shows a rapid reassembly upon return to neutral pH 7.0, accompanied by folding, followed by a slow phase in which the final 24-mer nanocage is formed.[20] Importantly, this fundamental work led to the rational redesign

https://doi.org/10.1021/acsomega.1c05472
ACS Omega 2022, 7, 823−836

of ferritin subunit interfaces, resulting in engineered nanocages capable of disassembly at a more amenable pH 4.0.[21] Such modification now permits labile compounds (e.g., small-molecule drugs) to be controllably loaded into ferritin nanocages in a facile and nondestructive manner, enabling downstream applications (e.g., drug delivery).[21]

In contrast, experimental data pertaining to encapsulins' ability to disassemble/reassemble and the mechanisms that underpin this natural phenomenon are sparse. The most characterized system is the $T = 1$ encapsulin from *Thermotoga maritima* (*Tm-Enc*), whose disassembly/reassembly has been primarily inspected via CD, polyacrylamide gel electrophoresis (PAGE), and TEM.[22] Specifically, *Tm-Enc* has been found to disassociate under strong acidic and alkaline conditions or at high concentrations of denaturing agents (e.g., guanidine hydrochloride, GuHCl). Furthermore, *Tm-Enc* was shown to spontaneously reassemble upon returning to the initial conditions (i.e., neutral pH or the absence of denaturants).[22,23] Interestingly, the reassembly of encapsulins in the presence of ESig-tagged cargo (e.g., proteins, nanomaterials) can enable selective encapsulation *in vitro*.[22−24] Based on these findings and the growing number of novel encapsulin structures, a better understanding of the biophysical mechanisms and physicochemical factors that underlie their disassembly/reassembly is needed. This includes characterizing the differences between structurally different encapsulins, specifically disassembly/reassembly conditions, reassembly timescales, and the impact these processes have on structural stability.

Motivated by this absence of information, we selected encapsulins with structures representing each of the three known architectures and then interrogated their disassembly/reassembly. These nanocages included *Tm-Enc* ($T = 1$) and the larger and more structurally complex encapsulins from *Myxococcus xanthus* (*Mx-Enc*, $T = 3$) and *Quasibacillus thermotolerans* (*Qt-Enc*, $T = 4$) which are less understood. We combined ITF spectroscopy, DLS, PAGE, and TEM to accurately monitor the assembly states of all three encapsulins under varying physicochemical conditions, including exposure to extreme pH, strong denaturants (GuHCl), and elevated temperatures. Furthermore, the effect disassembly/reassembly had on the nanocages' structural integrity was evaluated by atomic force microscopy (AFM). Together, this work presents critical insights into the dynamic mechanisms that govern the disassembly/reassembly of different encapsulin structures, which will help to expedite and broaden their future design, modification, and practical applications.

RESULTS AND DISCUSSION

Monitoring Encapsulin Assembly/Disassembly Using ITF Spectroscopy. Unloaded *Tm-Enc*, *Mx-Enc*, and *Qt-Enc* were produced in *Escherichia coli* and purified by size exclusion chromatography (SEC) and anion-exchange chromatography prior to biophysical characterization. Purification and correct self-assembly were confirmed using sodium dodecyl sulfate polyacrylamide gel electrophoresis (SDS-PAGE), blue native-PAGE, DLS, and TEM (Figures 2g and S1). TEM images of self-assembled *Tm-Enc*, *Mx-Enc*, and *Qt-Enc* displayed structures with a consistent shape and size (Figure 2g), and DLS analysis indicated a diameter of 23.7 ± 4.9 nm for *Tm-Enc*, consistent with its crystal structure data,[5] and a diameter of 32.0 ± 6.0 nm for *Mx-Enc* and 38.1 ± 7.3 nm for *Qt-Enc*, consistent with their cryogenic electron microscopy (cryo-EM) structures.[6,8] *Mx-Enc* was produced primarily in its $T = 3$ structure; however, populations of smaller, $T = 1$ like, structures were evident in Native-PAGE and TEM results (∼18 nm) (Figures S1 and 2g). This variation in the size of *Mx-Enc* has been previously observed, where recombinantly produced *Mx-Enc* without the presence of ESig-tagged cargo will form heterogeneous $T = 1$ and $T = 3$ populations.[8]

ITF spectroscopy is extremely sensitive to the local environment. As such, protein unfolding, disassembly, or conformational transitions often result in a change in the emission spectra of the Trp(s) within a protein, a lower maximum wavelength (blue-shifted) when the Trp(s) are buried, and a higher maximum wavelength (red-shifted) when solvent-exposed.[25]

Encapsulin subunits adopt a HK97-fold and have three conserved structural regions, a peripheral (P)-domain, an axial (A)-domain, and an elongated (E)-loop region (Figure S2).[3,4] Conveniently, each subunit of *Tm-Enc*, *Mx-Enc*, and *Qt-Enc* contains five, three, and two Trp residues, respectively. For each encapsulin, at least one of these Trp's is located within the interface between subunits, and one is located within the hydrophobic core of a single subunit (Figure 1a−c). Therefore, these intrinsic Trp residues are likely to be suitable reporters for both assembly/disassembly of the encapsulin macrostructure (i.e., tertiary/quaternary structure) and folding of the individual subunit polypeptide chains. Indeed, ITF spectroscopy has previously been used to monitor the refolding of $T = 1$ encapsulin from *Rhodococcus erythropolis* N771 when desorbed from a zeolite substrate.[26] ITF spectroscopy is also an appealing technique to monitor the process of encapsulin assembly/disassembly owing to its relative simplicity and its ability to report on a dynamic ensemble of structures in solution due to its nondestructive nature, which enables measurements to be performed in real time and allows the same sample to be subject to additional techniques. ITF spectroscopy also provides a method to monitor encapsulins in more complex physiological solutions, such as blood, which would be beneficial in investigating their biomedical potential. Additionally, unlike fluorescence resonance energy transfer-based techniques, ITF spectroscopy does not require modification of the protein with any extrinsic labels that may alter the assembly/disassembly dynamics.

Figure 1 shows the ITF spectroscopy of assembled *Tm-Enc*, *Mx-Enc*, and *Qt-Enc* overlayed with the spectra obtained after 1 h of incubation with 7 M GuHCl. For all three assembled encapsulins, blue-shifted Trp fluorescence spectra are observed (a ∼334 nm maximum emission wavelength for *Tm-Enc* and *Qt-Enc* and ∼338 nm for *Mx-Enc*), while in the presence of 7 M GuHCl, a dramatic red shift of the fluorescence spectra is seen (∼354 nm maximum emission wavelength). A maximum emission wavelength over 350 nm is observed, where the Trp's within a protein are completely solvent-exposed, as in an unfolded polypeptide chain.[27] Therefore, it appears that 7 M GuHCl fully disassembles *Tm-Enc*, as has previously been demonstrated,[22] as well as both *Mx-Enc* and *Qt-Enc*, by completely unfolding the protein.

It is also interesting to note that the overall fluorescence emission spectral shape represents an average of all Trp environments present in the protein.[28] Where a protein contains multiple Trp's, these may exist in different environments and therefore emit at different wavelengths. While we cannot draw conclusions about the foldedness/assembly of *Tm-Enc*, *Mx-Enc*, and *Qt-Enc* relative to one another (as they

https://doi.org/10.1021/acsomega.1c05472
ACS Omega 2022, 7, 823−836

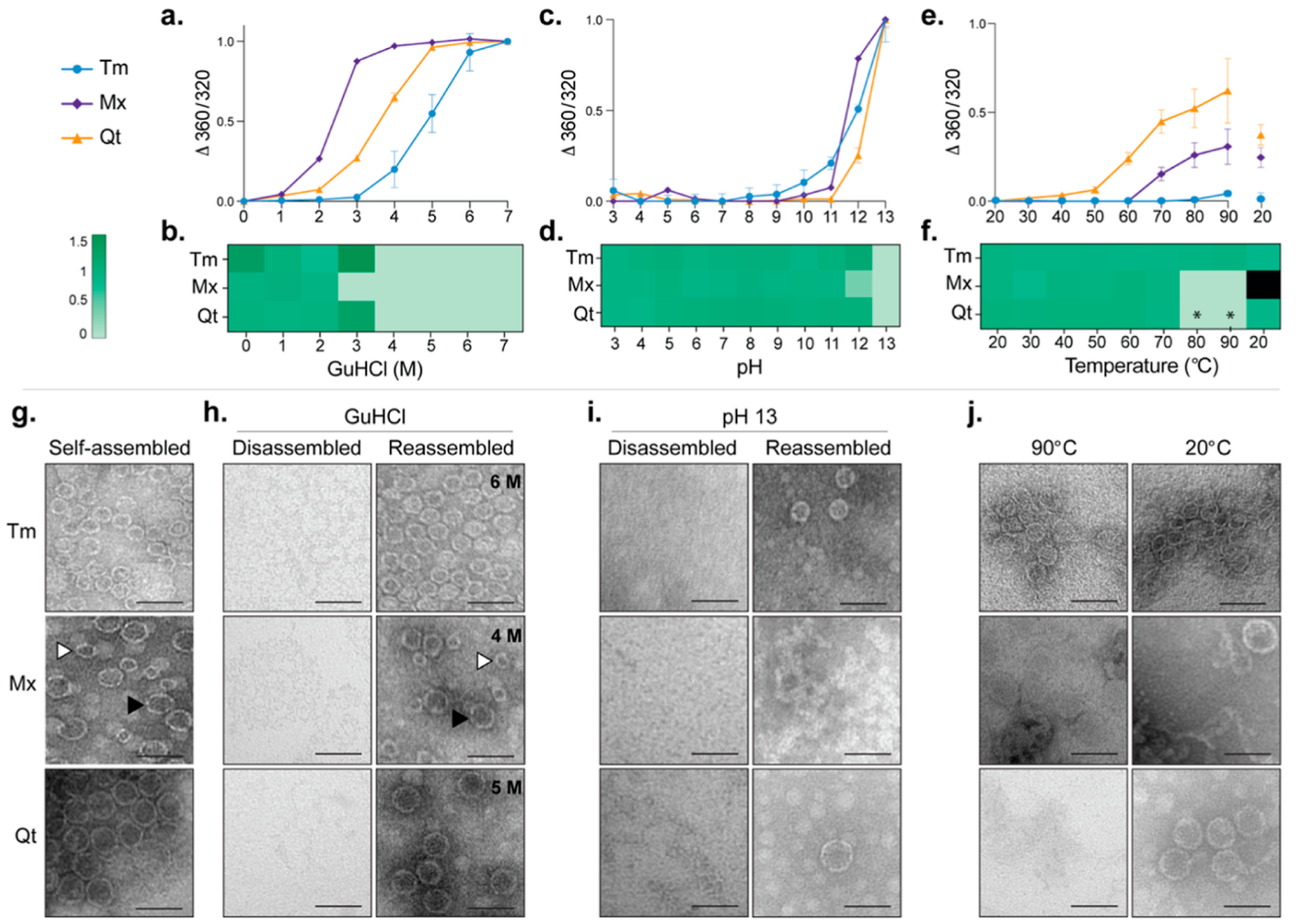

Figure 2. GuHCl, pH, and thermally induced disassembly of encapsulins. (a) ITF spectroscopy showed an observed shift in the emission wavelength (360/320) and indicated that Trp solvation begins from 1 M GuHCl for *Mx-Enc* and *Qt-Enc* and from 3 M for *Tm-Enc*. (b) DLS measurements indicated that *Mx-Enc* disassembled into its subunits (<0.5 nm) from 3 M GuHCl, and *Tm-Enc* and *Qt-Enc* disassembled from 4 M GuHCl. (c) ITF spectroscopy showed that Trp solvation increased significantly only under alkaline conditions from pH 12 for *Tm-Enc*, *Mx-Enc*, and *Qt-Enc*. (d) DLS measurements indicated that *Mx-Enc* began to disassemble at pH 12 (~13 nm) and all Enc disassembled into their subunits at pH 13 (<0.7 nm). (e) ITF emission wavelengths (360/320) of Enc between 20 and 90 °C and cooled back to 20 °C. *Tm-Enc* remained stable with slight Trp solvation from 80 °C that reversed when cooled back to 20 °C. *Mx-Enc* began to display Trp solvation from 60 °C and *Qt-Enc* from 40 °C. (f) DLS measurements show that *Tm-Enc* remained assembled to 90 °C, and *Mx-Enc* and *Qt-Enc* began to disassemble into their subunits (<0.5 nm) at 80 °C. *A smaller population of intermediate *Qt-Enc* structures that remained at 80−90 °C. Upon cooling to 90 °C, *Qt-Enc* appeared to reassemble, whereas *Mx-Enc* became aggregated (indicated by the black square). (g−j) TEM images show "self-assembled" encapsulins compared to those "disassembled" (i.e., complete absence of visible nanocage structures) under varying conditions and then "reassembled" back into spherical nanocages; *Mx-Enc* (black triangle $T = 3$, white triangle $T = 1$) (scale bars = 50 nm). For ITF data, the difference in the emission wavelength of complete Trp solvation (normalized to 1) and assembled Enc (normalized to 0) was plotted. Error bars represent the mean ± standard deviation; $n = 3$ from three independent experiments. DLS results were normalized so that 1 = expected assembled size and 0 = disassembled encapsulin.

all contain a different number of Trp's), changes in the spectral shape for the same encapsulin may discern encapsulin assembly (i.e., interactions between subunits) as opposed to the folding of individual subunit polypeptide chains. This is particularly true for *Qt-Enc*. As can be seen in Figure 1f, the peak shape for assembled *Qt-Enc* is flattened. This is consistent with its two Trp residues being located in different solvation environments such that in the spectra, two Trp's overlap but are not resolved (i.e., Trp95 being more buried in a helix at the pentamer/hexamer interface than Trp154, which is located on a loop in the A-domain, nestled within the hydrophobic core of a single *Qt-Enc* subunit) (Figures 1c and S2).

Instead of reporting the maximum fluorescence wavelength, herein, we have presented much of our ITF data as a fluorescence intensity ratio of emission at 360 and 320 nm (360/320). This ratio is used as a proxy for the shift in overall Trp fluorescence emission peak and avoids any bias arising from the spectral peak shape.[29] This approach has allowed us to expand the repertoire of methods that can be combined to monitor encapsulin assembly/disassembly across a range of conditions.

GuHCl-Induced Encapsulin Disassembly. GuHCl is a denaturant that affects the protein structure by disrupting noncovalent interactions, including hydrogen bonding and hydrophobic effects.[31] Our initial ITF spectroscopy results indicated that 7 M GuHCl completely unfolds the *Tm-Enc*, *Qt-Enc*, and *Mx-Enc* protein polypeptide chains (Figure 1) and thus disassembles the encapsulin macrostructure. To further examine the effect of GuHCl on encapsulin folding and assembly, all encapsulins were incubated in varying concentrations of GuHCl (0−7 M) for 1 h before performing ITF and DLS analyses.

https://doi.org/10.1021/acsomega.1c05472
ACS Omega 2022, 7, 823−836

The observed shift in the Trp emission peak for *Tm-Enc*, *Mx-Enc*, and *Qt-Enc* in the presence of GuHCl is shown in Figure 2a. As expected from our previous results, all three encapsulins show a blue to red shift from the assembled (0 M GuHCl, Δ360/320 = 0) to unfolded state (7 M GuHCl, Δ360/320 = 1). However, the concentration of GuHCl at which this transition occurs varies significantly between the different encapsulins. *Tm-Enc* Trp solvation began from approximately 3 M GuHCl, with complete Trp solvation from 6 M GuHCl, while *Mx-Enc* and *Qt-Enc* Trp solvation began at a lower concentration of 1 M GuHCl, with complete Trp solvation from 4 and 5 M GuHCl, respectively. This variation may reflect structural complexity, with the smaller and pentameric *Tm-Enc* being the most robust to GuHCl compared to the larger pentameric and hexameric *Mx-Enc* and *Qt-Enc*.

To complement these ITF spectroscopy results, DLS analysis was performed to characterize the size distribution of encapsulins in solution for the same samples (Figure 2b, Table S2). For *Mx-Enc*, no intact encapsulin macrostructure is detectable by DLS at concentrations ≥3 M GuHCl, which also correlates with the significant red-shifted Trp emission at 3 M GuHCl (Δ360/320 = 0.88). This result suggests that *Mx-Enc* is both disassembled and largely unfolded at GuHCl concentrations ≥3 M. However, for *Tm-Enc* and *Qt-Enc*, the absence of the intact encapsulin macrostructure occurs at lower GuHCl concentrations than the major red shift in Trp emission. For example, at 4 M GuHCl, the *Tm-Enc* macrostructure is not detectable by DLS, but the Trp emission remains significantly blue-shifted (Δ360/320 = 0.20), corresponding to a native-like fold. A similar result is seen for *Qt-Enc* at 3 M GuHCl (Δ360/320 = 0.27). TEM and native-PAGE images of each encapsulin after incubation in the lowest GuHCl concentration required for significant Trp solvation also show the absence of nanocage macrostructures, confirming their disassembly. Upon dialysis in the reassembly buffer (50 mM HEPES, 1 mM DTT) overnight, all three encapsulins subsequently reassembled into their original macrostructure (Figures 2h, S4, and S3).

Taken together, these results point to the existence of an intermediate state(s) in *Tm-Enc* and *Qt-Enc* GuHCl-induced disassembly, in which the nanocage breaks down into smaller (<0.5 nm) entities with a native-like fold. There is insufficient evidence from ITF or DLS analysis to define the stoichiometry or structure of this intermediate state(s). However, a previous native mass spectrometry study of the $T = 1$ encapsulin from *Brevibacterium linens* suggested that reassembly occurs via the formation of stable dimers prior to the final nanocage.[32] It is possible that disassembly of *Tm-Enc* and *Qt-Enc* proceeds via a similar mechanism. We also cannot rule out that *Mx-Enc* proceeds via an equivalent intermediate state upon GuHCl-induced disassembly. However, if this is the case, our data suggest that the chemical stability of the nanocage and the intermediate for *Mx-Enc* are more closely matched, and less chemically stable, than those of *Tm-Enc* or *Qt-Enc* such that both disassembly and complete unfolding occur at close to 3 M GuHCl. This potential model of encapsulin disassembly warrants further investigation as disassembly of the nanocage utilizing lower GuHCl concentrations, without completely unfolding the encapsulin protein, may provide an effective scheme for loading and/or releasing more chemically sensitive cargo.

Overall, our results for GuHCl-induced encapsulin disassembly suggest that folding plays a critical role for encapsulin nanocage assembly/disassembly. The smaller, less complex *Tm-Enc* structure requires more GuHCl for unfolding than the larger, more complex *Qt-Enc* and *Mx-Enc*. This agrees with the difference in the high stability of ferritin, which is a small protein nanocage comprising 24 subunits, compared to the high sensitivity of larger and more structurally complex VLPs in denaturants. Ferritin is stable up to 6 M GuHCl[33] and requires 8 M of the denaturant urea for disassembly.[34] A concentration of 2 M GuHCl is not strong enough to disassemble ferritin but is able to unfold the α-helices surrounding ferritin channels, thereby enlarging its pores to allow entry of cargo without the need for complete disassembly.[35] Contrastingly, the larger P22 VLP, which assembles from 420 subunits into a $T = 7$ nanoparticle-like structure that is 56 nm in diameter, dissociates at just 3 M GuHCl.[36] However, the chemical stability of the encapsulins tested is not directly related to their size as *Qt-Enc* requires more GuHCl for unfolding than the smaller *Mx-Enc*. Hence, other factors, such as the symmetry and stability of intermediate state(s), also need to be taken into consideration.

pH-Induced Encapsulin Disassembly. To investigate the role of electrostatic interactions in maintaining the encapsulin macrostructure, ITF and DLS analyses were also performed for the three encapsulins at varying pH (Figure 2c,d). The theoretical pI of *Tm-Enc*, *Mx-Enc*, and *Qt-Enc* are 4.90, 5.45, and 5.02, respectively.[37] If electrostatic interactions play a major role in the mechanism of encapsulin assembly, we would expect to see disassembly of the encapsulin nanocage at pH < pI (where the overall charge on the protein would be positive rather than negative, as at neutral pH). However, this is not the case. ITF spectroscopy indicates that all encapsulins remain relatively stable across a broad pH range, with a significant change in Trp exposure only observed under extreme alkaline conditions (pH 12−13) (Figure 2c). DLS demonstrates the presence of assembled encapsulins at all pHs, with the exception of pH 13, and smaller structures (∼13 nm) at pH 12 for *Mx-Enc* (Figure 2d, Table S3). Disassembly of the nanocage structures at pH 13 was also confirmed by TEM (Figure 2i). These results support a recent study that used Native-PAGE analysis to confirm that *Qt-Enc* is stable between pH 4.5 and 8.5.[24] Therefore, loss of electrostatic interactions between and/or within encapsulin subunits is unlikely to be a major driving force for disassembly. Disassembly more likely arises at extreme alkaline pH due to deprotonation of the protein side chains, resulting in a loss of the hydrogen bonding that holds the protein scaffold together.[38]

Thermal Encapsulin Disassembly. To assess encapsulin thermostability, assembled samples were heated to 90 °C with ITF and DLS measurements taken every 10 °C up to 90 °C as well as upon return to 20 °C. Additionally, encapsulins were heated to 90 °C with TEM samples prepared both immediately after heating and after being cooled at 20 °C for 1 h. ITF results showed that the *Tm-Enc* encapsulin remained stable throughout heating, with only a very slight red shift in the emission wavelength observed at temperatures above 80 °C, which was recovered when cooled back to 20 °C (Figure 2e). No significant change in the size of the *Tm-Enc* nanocages was observed by DLS, and TEM images showed assembled cages after heating to 90 °C, suggesting that the *Tm-Enc* nanocage is resistant to thermal disassembly (Figures 2f,j and S4; Table S4).

https://doi.org/10.1021/acsomega.1c05472
ACS Omega 2022, 7, 823−836

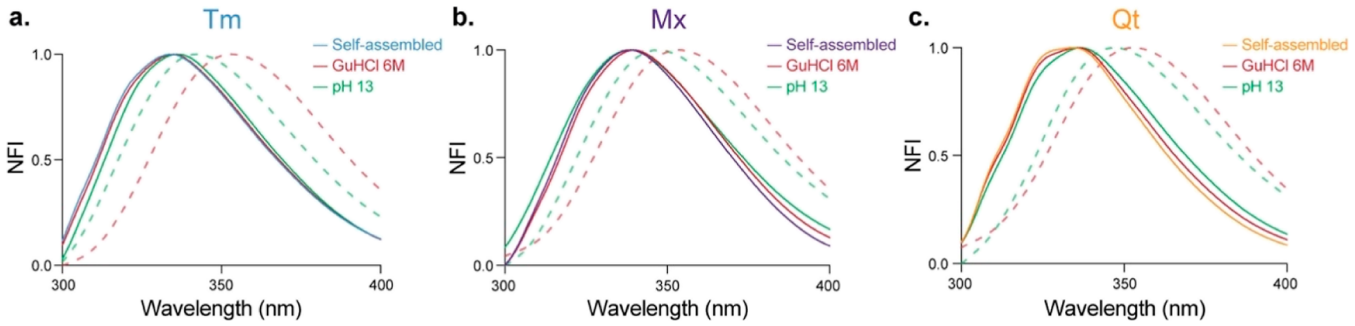

Figure 3. Comparison of Enc spectra of self-assembly, disassembly in 6 M GuHCl or at pH 13, and subsequent reassembly. (a) *Tm-Enc* ITF emission when self-assembled (blue), disassembled with 6 M GuHCl (dotted red), reassembled after 6 M GuHCl disassembly (solid red), disassembled with pH 13 (dotted green), and reassembled after pH 13 disassembly (solid green). (b) *Mx-Enc* ITF emission when self-assembled (purple), disassembled with 6 M GuHCl (dotted red), reassembled after 6 M GuHCl disassembly (solid red), disassembled with pH 13 (dotted green), and reassembled after pH 13 disassembly (solid green). (c) *Qt-Enc* ITF emission when self-assembled (orange), disassembled with 6 M GuHCl (dotted red), reassembled after 6 M GuHCl disassembly (solid red), disassembled with pH 13 (dotted green), and reassembled after pH 13 disassembly (solid green). NFI was achieved by making the maximum Trp emission wavelength (nm) = 1.

In contrast to *Tm-Enc*, both *Mx-Enc* and *Qt-Enc* disassemble at elevated temperatures. *Mx-Enc* Trp solvation began from 60 °C and disassembled from 80 °C, as shown by DLS (Figure 2e,f, Table S4) and appeared disassembled at 90 °C via TEM imaging (Figure 2j). Additionally, in contrast to *Tm-Enc*, disassembly of *Mx-Enc* by temperature is not reversible as when cooled back to 20 °C, only large aggregates were found (Figure 2f, Table S4). Similarly, ITF spectroscopy showed *Qt-Enc* began Trp solvation from 40 °C, and DLS indicated that the majority of the sample disassembled at 80 and 90 °C. However, even at 90 °C, a smaller population (approx. 16%) of *Qt-Enc* subunits remained in intermediate structures of ∼14 nm and another population (approx. 16%) at the assembled size of ∼44 nm (Figures 2f and S4; Table S4). When cooled back to 20 °C, DLS and TEM indicated that *Qt-Enc* reassembled primarily back into its original size (DLS data also showed a smaller population of approx. 32% at ∼15 nm) and ITF spectroscopy showed a blue shift of emission (Figure 2e,f,j and S4; Table S4).

The difference in the thermal stability and reassembly of *Tm-Enc*, *Mx-Enc*, and *Qt-Enc* points to kinetic complexity in the encapsulin assembly pathway. For *Mx-Enc*, aggregation of the unfolded/disassembled state is likely the main obstacle to achieving proper reassembly. Our GuHCl data also suggest that the *Mx-Enc* unfolded/disassembled state(s) is less stable than for *Tm-Enc* or *Qt-Enc*. While *Qt-Enc* began Trp solvation at 40 °C, DLS showed that it did not change in size until 80 °C, indicating that *Qt-Enc* undergoes structural change from 40 °C but remains assembled until 80 °C. The stabilities of *Tm-Enc* and *Qt-Enc* at high temperatures are consistent with them being derived from thermophilic bacteria.[5,6] However, *Mx-Enc* is derived from bacteria that live in soil,[39] which may explain its lower tolerance to temperature.

Alternate Disassembly Conditions. We have begun to use the ITF technique, developed herein, to investigate other chemical additives that may alter the folding and/or assembly of encapsulins, including redox conditions (10 mM DTT or H_2O_2) and ionic environments (1 M NaCl). However, we are yet to find another condition to induce disassembly. All encapsulins remained stable in NaCl, and only *Mx-Enc* displayed a small blue shift in emission in H_2O_2 and an observable increase in diameter after incubation in either DTT or H_2O_2 (Figure S5, Table S7). This may be due to reduction/oxidation of disulfide bonds causing a weaker association between subunits, resulting in swelling of the nanocage.[40]

Encapsulin Reassembly. Based on the above results, high concentrations (6 M) of GuHCl and pH 13 conditions were selected for further analysis of the *Tm-Enc*, *Mx-Enc*, and *Qt-Enc* reassembly mechanism. Notably, these conditions disassemble encapsulins to differing degrees. ITF spectroscopy revealed maximum peak emissions for disassembly with pH 13 to be ∼341 nm for *Tm-Enc* and ∼347 nm for *Mx-Enc* and *Qt-Enc*, whereas disassembly with 6 M GuHCl resulted in a maximum peak emission at ∼354 nm for all encapsulins (Figure 3a−c). As previously discussed, a Trp emission maximum ≥350 nm (as observed for all encapsulins in 6 M GuHCl) is expected for the unfolded protein. However, at pH 13, all encapsulins display a Trp max emission <350 nm, suggesting that at least some of their subunits' secondary structure remains intact.

Reassembly of all encapsulins after disassembly in either 6 M GuHCl or pH 13 was initiated via overnight dialysis into the reassembly buffer. Following disassembly in 6 M GuHCl, *Tm-Enc*, *Mx-Enc*, and *Qt-Enc* all reassembled back to their original structures, as indicated by ITF maximum emission and DLS size (Figures 3a−c and S4). In contrast, after disassembly in pH 13, only *Tm-Enc* reassembled to its original structure. For *Mx-Enc* and *Qt-Enc*, a blue shift in ITF emission, resembling the Trp maximum emission of the original self-assembled material, was observed. However, native-PAGE results showed no bands (Figure S3), and TEM analysis found no structures for *Mx-Enc*, and only a single nanocage was imaged for *Qt-Enc* (Figure 2i). Indeed, DLS analysis of pH 13 reassembled *Mx-Enc* and *Qt-Enc* showed the presence of either large aggregates or smaller structures (∼18 nm for *Mx-Enc* and ∼9−25 nm for *Qt-Enc* Figure S4), which suggests that the subunits may be reassembling into smaller cages and/or intermediate structures at a concentration too low to detect by native-PAGE and TEM.

As previously discussed, at pH 13, hydrolysis of the peptide bonds can occur, leading to protein misfolding and/or aggregation,[38] which may account for some of this inefficiency in encapsulin reassembly. Interestingly, although the position of the Trp emission peak for the original self-assembled, GuHCl reassembled, and pH 13 reassembled samples of *Qt-Enc* is not significantly different, a difference in spectral shape is noted for the pH 13 reassembled sample. The blue-shifted shoulder of the *Qt-Enc* Trp emission peak, which is thought to

https://doi.org/10.1021/acsomega.1c05472
ACS Omega 2022, 7, 823−836

correspond to Trp95 buried in the pentamer/hexamer interface of the intact nanocage, is lower in intensity for the pH 13 reassembled sample. This result is consistent with reassembly of a different structure with a native-like fold, instead of the original intact $T = 4$ *Qt-Enc* nanocage, upon reassembly from pH 13. The reassembly of *Mx-Enc* and *Qt-Enc* after pH 13 disassembly into smaller nanocages and/or alternative structures in inefficient quantities suggests that this pathway, in its native form, may not be suitable for some applications.

Timescale of Encapsulin Reassembly. To advance encapsulins as a cargo-carrying platform, the disassembled encapsulin needs to be able to be reassembled on a viable timescale. As the assembly rate of encapsulins inside host cells (native or recombinant) cannot be accurately monitored, *in vitro* reassembly can provide insights into their self-assembly *in vivo*. The encapsulin nanocages were disassembled for 1 h via 6 M GuHCl or pH 13 before reassembly was initiated using dialysis, with samples measured by ITF and DLS analyses every 15 min over a 75 min time frame. The rate of reassembly appeared to vary between each Enc. *Tm-Enc* reassembled faster than *Mx-Enc* and *Qt-Enc*, with DLS indicating that *Tm-Enc* reached its assembled diameter within 15 min after being disassembled via pH 13 and between 15 and 30 min when disassembled via 6 M GuHCl (Figure 4a,b, Tables S5 and S6). The faster reassembly after pH 13 disassembly compared to GuHCl may be explained by the subunits still maintaining some structure after incubation under pH 13 conditions. However, *Tm-Enc* reassembly after pH 13 disassembly displayed a more gradual Trp burial and a slight decrease in size at 45 min (Figure 4a,b, Table S6). This suggests that reassembly after pH 13 may follow a more dynamic pathway, with rapid nanocage formation, followed by restructuring. In contrast, after 6 M GuHCl disassembly, *Qt-Enc* reassembled into its original diameter between 30 and 45 min, and *Mx-Enc* appeared to partially assemble between 45 and 60 min but only completely assembled between 60 and 75 min (Figure 4a,b, Table S5). The difference in rates between encapsulins may reflect the overall stability of the complex; that is, complexes that are more stable may reassemble quicker. In a recent report, the *in vivo* loading of cargo proteins into *Tm-Enc* during its self-assembly was found to be ∼8 times less efficient than with *Mx-Enc*.[41] The authors suggested that this striking difference was partly due to the smaller *Tm-Enc* self-assembling at a faster rate than *Mx-Enc*, thus limiting the available contact time between ESig-tagged cargo and the nanocage's interior surface. This hypothesis is now supported by our observation that *Tm-Enc* reassembles up to 4 times quicker than the larger *Mx-Enc* (Figure 4). This therefore highlights the critical role assembly time frames play in cargo-loading efficiency and that modifying such properties can enhance cargo packing, density, and/or stoichiometry.

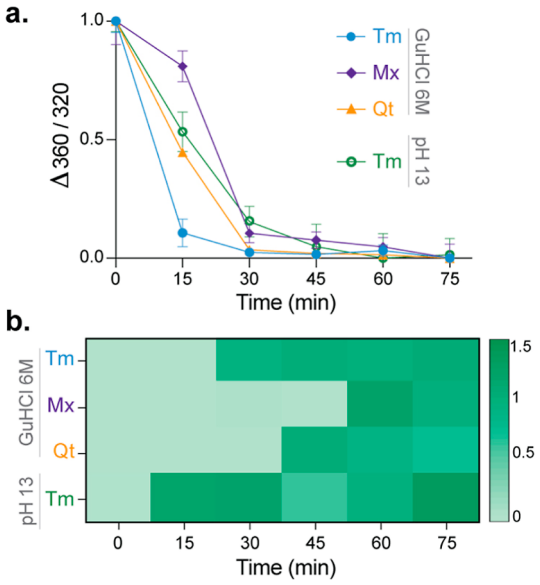

Figure 4. Reassembly time frames of encapsulins. (a) ITF spectral shift in the emission wavelength (Δ360/320) of *Tm-Enc*, *Mx-Enc*, and *Qt-Enc* disassembled via 6 M GuHCl and *Tm-Enc* disassembled via pH 13 and reassembly measured every 15 min. The difference in the emission wavelength of disassembled encapsulin (normalized to 1) and assembled encapsulin at 75 min (normalized to 0) was plotted. Error bars represent the mean ± standard deviation; $n = 3$ from three independent experiments. (b) Heat map of DLS measurements of *Tm-Enc*, *Mx-Enc*, and *Qt-Enc* disassembled via 6 M GuHCl and *Tm-Enc* disassembled via pH 13 and reassembly measured every 15 min. DLS results were normalized so that 1 = expected assembled size and 0 = disassembled encapsulin.

The rapid burial of Trp residues for all encapsulins within 15 min, as shown by ITF spectroscopy, prior to the formation of the cages, suggests a reassembly pathway where subunits first fold into an intermediate structure before gradually forming the cage. A previous study on encapsulins from *B. linens* ($T = 1$) suggested that reassembly occurred with subunits first forming stable dimers prior to the final nanocage formation, with a preference for even-numbered stoichiometries as demonstrated via mass spectrometry analysis.[32] Additionally, ferritin has been found to have a biphasic reassembly, where an initial fast step occurs with folding of subunits and unknown stable intermediates, followed by the slower restructuring of intermediates into the nanocage.[20]

Data of the pH 13 reassembly rate for *Mx-Enc* and *Qt-Enc* were not included as the presence of aggregation prevented extraction of accurate DLS size values. This suggests that reassembly from the pH 13 disassembled state for the larger and more complex *Mx-Enc* and *Qt-Enc* may be prone to protein misfolding pathways and/or partial assembly and thus, without additional re-engineering, may not be ideal for use in future applications.

These results also highlight the value of adding ITF spectroscopy to complement the existing repertoire of methods to monitor disassembly/reassembly of encapsulins. Although CD may provide more specific secondary structural information, ITF spectroscopy can monitor global structural changes (i.e., tertiary/quaternary) due to information about the degree of local solvation.[42] This may be a more genuine representation of encapsulin macrostructure assembly. In addition, unlike ITF spectroscopy, CD spectroscopy is not compatible with the high concentration of GuHCl required to completely unfold encapsulins.[43]

Nanomechanical Stability of Self-Assembled versus Reassembled Encapsulins. To understand any changes in the structural integrity of *Tm-Enc*, *Mx-Enc*, and *Qt-Enc* after reassembly under the conditions tested above, AFM was utilized to compare the morphology, rupture point, and elasticity between self-assembled and reassembled encapsulins. As the future application of encapsulins will likely require native solution conditions, it was pertinent to examine their structural integrity in solution and is why AFM was utilized

https://doi.org/10.1021/acsomega.1c05472
ACS Omega 2022, 7, 823−836

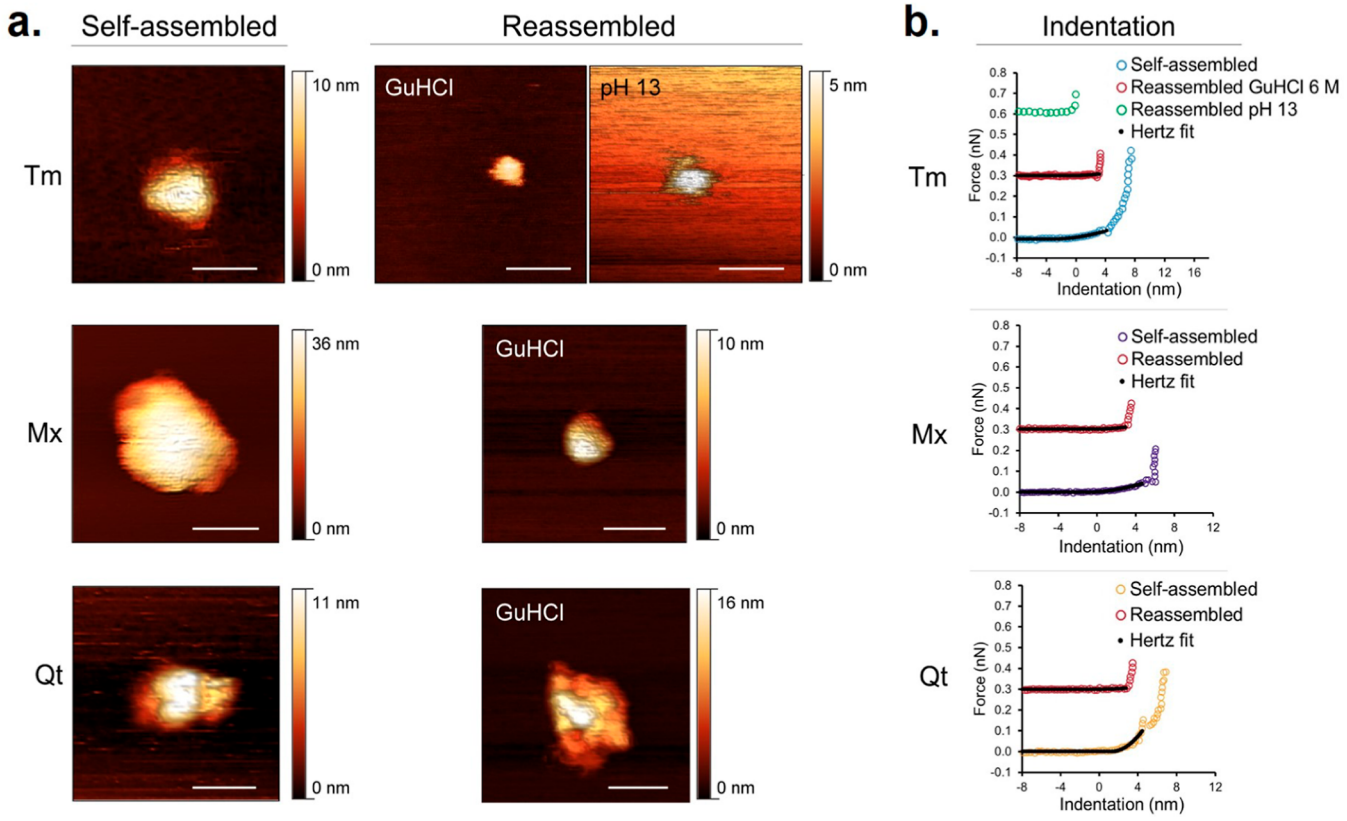

Figure 5. AFM imaging and elasticity comparing self-assembled/reassembled encapsulins. (a) Nanoscale AFM images obtained for individual encapsulins comparing the morphologies of self-assembled *Tm-Enc*, *Mx-Enc*, and *Qt-Enc* with encapsulins disassembled via pH 13 or GuHCl (6 M) and subsequently reassembled. White scale bars represent 30 nm. (b) Representative indentation curves and the Hertz fit of encapsulins used to determine Young's elastic modulus (E) using the Hertz equation to convert experimentally derived force versus distance curves into indentation data (colored circles) and to fit the elastic (nonlinear) region to calculated *E* values (black lines).

over alternative techniques that examine proteins in the gas phase, such as native mass spectrometry. AFM has been employed to assess the mechanical stability of comparable bacterial microcompartments (i.e., carboxysomes)[44] and VLPs.[52] Indeed, previous AFM analysis has been done on the rigidity of *Tm-Enc* and encapsulins from *B. linens* ($T = 1$) and suggested that the presence of cargo within encapsulins from *B. linens* may lead to some destabilization, as indicated by a lower rupture force in loaded versus unloaded encapsulins.[32] However, the effect of reassembly on the nanomechanical stability on *Tm-Enc* as well as the larger and more structurally complex *Mx-Enc* and *Qt-Enc* is yet to be elucidated.

Individual encapsulins were imaged with a scan size of ∼100 nm × 100 nm to visualize their topographical detail. Self-assembled encapsulins were found to be at their expected size (*Tm-Enc*, 24 nm; *Qt-Enc*, 42 nm), including both the $T = 3$ (32 nm) and $T = 1$ (17 nm) conformations of *Mx-Enc* (Figure 5a). However, clear morphological variation can be seen after reassembly, with all encapsulins demonstrating flattening of their surfaces. Additionally, *Qt-Enc* appeared more aggregated after reassembly.

Being composed of similar constituents, approximately the same elasticity would be expected between each self-assembled encapsulin, which was found to be the case of *Tm-Enc* and *Mx-Enc*, with an average elasticity of 2.77 ± 0.96 and 2.12 ± 0.81 MPa, respectively (Figures 5b and S6). However, *Qt-Enc* displayed a higher average elasticity of 25.60 ± 14.92 MPa, indicating that it has greater structural integrity and is therefore more resilient to deformation (Figures 5b and S6). *Qt-Enc* may therefore be more strongly self-assembled than *Tm-Enc* and *Mx-Enc*, which could be attributed to its higher structural complexity, as the different symmetries and subunit−subunit contacts may influence the strength of interfacial interactions.[45] Upon reassembly following 6 M GuHCl disassembly, the elasticity of all encapsulins decreased significantly, with a *Tm-Enc* average elasticity of 1.16 ± 0.93 MPa (58.12% decrease), *Mx-Enc* 1.39 ± 0.78 MPa (34.43% decrease), and *Qt-Enc* 0.85 ± 0.62 MPa (96.68% decrease), indicating a significant reduction in structural integrity (Figure 5b and S6). Elasticity data of reassembled *Tm-Enc* after disassembly via pH 13 were not included as during testing, the sample became unstructured and did not retain any elasticity or show any elastic response. This suggests that even though *Tm-Enc* reassembled after disassembly via pH 13, these conditions may have irreversibly altered the protein by hydrolysis, thereby affecting stability.[38]

The rupture force represents the maximum force a protein cage withstands prior to puncture by the AFM tip.[46] The rupture force of all self-assembled encapsulins was between ∼0.1 and 0.2 nN, indicating that they are fairly fragile (Figure 5b). This is in contrast to AFM results from a previous study on self-assembled empty *Tm-Enc* and encapsulins from *B. linens*, which had rupture forces of 0.63 and 0.64 nN, respectively,[32] indicating that the encapsulins used in the current study are slightly more fragile. After reassembly, the rupture force decreased further by a factor of ∼5 for each encapsulin system tested (Figure 5b).

https://doi.org/10.1021/acsomega.1c05472
ACS Omega 2022, 7, 823−836

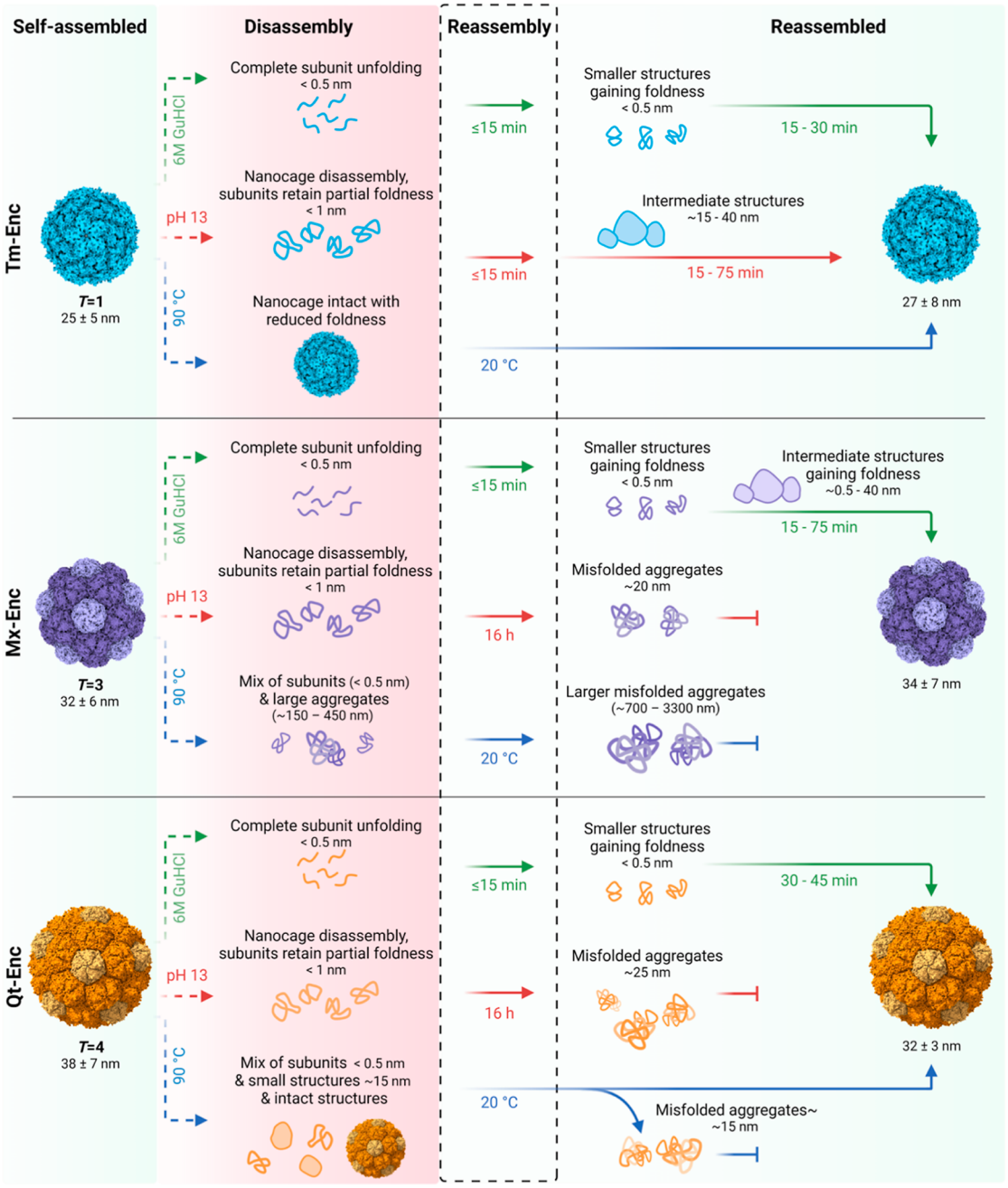

Figure 6. Proposed disassembly/reassembly pathways for each encapsulin architecture. Schematic diagram that compares and contrasts the proposed disassembly/reassembly dynamics, pathways, timescales, and potential intermediates of the three encapsulin architectures, as elucidated from our results. Encapsulin size was determined by DLS, and foldedness was based on ITF results.

Together, these results show that after undergoing disassembly in either 6 M GuHCl or pH 13 and subsequent reassembly, all three encapsulin architectures significantly lose structural integrity. In terms of encapsulins loaded with cargo under *in vitro* conditions, the observed increased fragility could be beneficial if wanting a system that can be easily broken down to release cargo, such as intracellular drug delivery or immunotherapy. If in need of a more robust system (e.g., enzyme-loaded nanocages for industrial biocatalysis), however, these results demonstrate the importance of understanding and modifying encapsulins, so they can disassemble under more specific and benign conditions. Accordingly, future encapsulin engineering efforts could focus on the site-directed modification of specific amino acids and/or key structural domains within subunits or at the interface between subunits (e.g., the E-loop domain) to trigger disassembly/reassembly. For example, recently, a GALA peptide was inserted in the E-loop region of *Qt-Enc* which underwent a coil-to-helix conformational change at pH 5.5, allowing triggered reversible disassembly under more facile conditions.[24] This work represents a promising step forward to controlling encapsulin assembly; however, further insights into how modifications affect cargo loading efficiency, reassembly speed, and functional cargo proteins are required for a fully developed stimuli-responsive loading approach. Therefore, our results may provide information that could assist in improving such strategies.

https://doi.org/10.1021/acsomega.1c05472
ACS Omega 2022, 7, 823−836

Furthermore, to enhance understanding of the reassembly pathway of encapsulins, future studies could assess real-time assembly of the subunits. This has been achieved by using AFM with large bacterial microcompartments, where it was revealed that the shell facets assemble from preformed oligomers,[47] and the pH-dependent disassembly/reassembly of ferritin has also been monitored in real space.[48] Similarly, highly specialized efforts by MS researchers to combine structural MS techniques (i.e., Native MS) to determine the real-time stepwise assembly of oligomeric protein cages are also ongoing.[49] Such strategies might be complemented with cryo-EM and SAX methods to further probe the dynamic transitions of intermediate structures within encapsulin disassembly/reassembly pathways. The data presented in this report provide a clear framework to relate structural transitions observed by such non-solution-based techniques to the process of Enc assembly/disassembly in solution.

CONCLUSIONS

In summary, this study determined a set of physicochemical conditions that induce the disassembly/reassembly of *Tm-Enc*, *Mx-Enc*, and *Qt-Enc*, with each encapsulin system showing varying degrees of sensitivity to denaturants, pH, and temperature. As shown in Figure 6, the data generated also revealed several structural states and changes (i.e., protein structure, size, and foldedness) that occur during the dynamic process of encapsulin disassembly/reassembly, with clear differences between the disassembly/reassembly pathways of all three encapsulin architectures studied. Using AFM, we revealed a previously unknown effect of *in vitro* disassembly/reassembly on encapsulin stability, finding that the encapsulin loses a substantial amount of structural integrity when disassembled and subsequently reassembled. These findings have implications if requiring *in vitro*-loaded encapsulins for a particular application but may be beneficial when nanocage dissociation and cargo release are favored.

At high concentrations of GuHCl, all three encapsulins completely unfold and refold efficiently; however, these harsh conditions pose limitations for applications involving *in vitro* loading of cargo that may be sensitive to these conditions as it could be destroyed in the process. Furthermore, the use of harsh denaturants and extreme pH to disassemble encapsulins may limit their downstream utility, especially in biomedicine, where biocompatibility is paramount. With an increased understanding of the encapsulin structure, disassembly/reassembly conditions, stability, and stoichiometry of intermediate structures and having established clear differences of these between the encapsulins assessed herein, this study provides the groundwork to test the effect of altering the native Enc sequences. For example, by identifying critical interactions between nanocage subunits that may affect the assembly process, future genetic engineering efforts of subunits may lead to enhanced control over conditions that trigger disassembly/reassembly, size, structure, and cargo-loading efficiency of encapsulins.[50,51]

In summary, the findings of this study advance our understanding of encapsulins by providing critical insight into their unique disassembly/reassembly dynamics. This knowledge provides a roadmap toward an encapsulin "tool kit" comprising nanocages with varying structural architectures and biochemical/biophysical properties, which can be readily selected and further customized for a specific nanobiotechnological application.

MATERIALS AND METHODS

Materials. All chemicals and reagents used in this study were purchased from Sigma-Aldrich unless stated otherwise.

Molecular Cloning of Constructs. All inserts were codon-optimized for expression in *E. coli* and custom-synthesized as gBlock Gene Fragments (Integrated DNA Technologies). Encapsulins from *T. maritima* (*Tm*) (UniProt: TM_0785), *M. xanthus* (*Mx*) (UniProt: MXAN_3556), and *Q. thermotolerans* (*Qt*) (UniProt: QY95_01592) were each synthesized with flanking restriction sites (NcoI/BamHI). For gene expression in *E. coli*, *Tm-Enc* was cloned into pETDuet-1 (Novagen, Merck), and *Mx-Enc* and *Qt-Enc* were cloned into pACYC-Duet-1 (Novagen, Merck), summarized in Table S1. *E. coli* α-Select (Bioline, UK) was used for general plasmid storage and propagation. Gene insertion was confirmed by PCR using primer pairs pETUpstream/DuetDOWN (Merk). *E. coli* BL21 (DE3) cells (New England Biolabs) were used for recombinant protein expression. Herein, cells were transformed with the appropriate plasmids, and the resulting transformants were selected on Luria−Bertani (LB) agar supplemented with either 100 mg/mL of carbenicillin or 50 mg/mL of chloramphenicol (see Table S1).

Recombinant Protein Production. Protein expression experiments were performed in the LB medium supplemented with carbenicillin (100 mg/mL) or chloramphenicol (50 mg/mL). Briefly, strains were streaked out on LB agar plates and grown overnight at 37 °C. A starter culture (1 colony in 5 mL LB) was grown for 16 h at 37 °C and used to inoculate 500 mL of LB media. Cultures were incubated at 37 °C with flasks shaking at 200−250 rpm until an optical density at 600 nm (OD600) of 0.5−0.6 was reached. Protein synthesis was then induced by the addition of isopropyl-β-*d*-thiogalactopyranoside (IPTG) to a final concentration of 0.1 mM. Induced cultures were incubated at 37 °C with flasks shaking at 200−250 rpm for 4 h and then cells were harvested via centrifugation (8000*g*, 4 °C, 15 min). The resulting cell pellets were stored at −30 °C until further use.

Protein Purification. Cell pellets from 500 mL encapsulin-producing cultures were thawed and resuspended in 30 mL of lysis buffer [50 mM 4-(2-hydroxyethyl)-1-piperazineethanesulfonic acid (HEPES) buffer, pH 7.4 (Chem-Supply Pty) and Benzonase nuclease 10 U/mL]. Cells were lysed by three rounds of passage through a French pressure cell at 1000 psi and centrifuged at 8000*g* and 4 °C for 15 min. The supernatant containing the soluble protein was heat-treated in a water bath at 65 °C for 15 min before centrifugation (10,000*g*, 4 °C, 10 min). Protein precipitation was initiated by adding 10% (w/v) PEG8000 and 2% (w/v) NaCl to the supernatant, followed by incubation on ice for 30 min. Next, the sample was spun down at 10,000*g* for 10 min at 4 °C. The precipitated protein was resuspended in 2.5 mL of HEPES buffer (50 mM, pH 7.4) and filtered through a 0.22 mm syringe filter.

All purifications were carried out on an ÄKTA start chromatography system (GE Healthcare). The three encapsulins used in this study were purified via SEC using a HiPrep 26/60 Sephacryl S-500 HR column (GE Healthcare) equilibrated with 50 mM HEPES pH 7.4. This column is traditionally used to separate large macromolecules and not typically used for proteins, however, this is the standard column used for encapsulins due to their large size.[6,13] Fractions showing the corresponding encapsulin band on SDS-PAGE were pooled and subjected to further purification

https://doi.org/10.1021/acsomega.1c05472
ACS Omega 2022, 7, 823−836

via anion-exchange chromatography using a HiPrep Q 16/10 column (GE Healthcare) equilibrated with 50 mM HEPES pH 7.4. Encapsulin proteins were eluted with a linear gradient of 0−0.3 M NaCl and 0.3−1 M NaCl (Figure S1). Fractions containing encapsulins, identified via SDS-PAGE, were pooled, concentrated, and buffer-exchanged into 50 mM HEPES buffer pH 7.4 using Amicon Ultra-15 centrifugal filter units with a 100 KDa cutoff. Last, purified encapsulin Enc proteins were filtered through a 0.22 mm syringe filter and stored at −30 °C until further use.

PAGE Analysis and Protein Quantification. Protein samples were denatured, separated, and visualized using SDS-PAGE, with molecular weights compared with a commercial protein ladder (Precision Plus Protein, BioRad). A Bio-Rad mini-protean system (Bio-Rad laboratories) was used for SDS-PAGE analysis. Protein samples were mixed in a 1:1 ratio with 2X Laemmli sample buffer with 50 mM 1,4-dithiothreitol and heated at 99 °C for 10 min with shaking at 300 rpm in a ThermoMixer (Eppendorf). Electrophoresis was performed at 200 V for 30 min on a 4−20% polyacrylamide gel (Mini-PROTEAN TGX, BioRad) in SDS running buffer (25 mM Tris, 192 mM glycine, 1% (w/v) SDS, pH 8.3). Gels were stained following the Coomassie G-250 safe stain protocol. Encapsulin assembly was visualized via nondenaturing Blue Native-PAGE (BN-PAGE). An XCell SureLock Mini-Cell Electrophoresis System (Thermo Fisher Scientific) was used for BN-PAGE analysis. Protein samples were mixed in a 1:4 ratio with 4× Native-PAGE sample buffer (Thermo Fisher Scientific) and loaded into NativePAGE 3−12% Bis-Tris protein gels (Thermo Fisher Scientific). BN-PAGE was performed using two different running buffers: 1× anode buffer (NativePAGE running buffer 20×, Thermo Fisher Scientific) in the outer buffer chamber and 1X dark-blue cathode buffer (1× anode buffer, 0.02% (w/v) Coomassie G-250) in the inner buffer chamber. Last, the samples were run on ice at 150 V for 90 min, followed by a second run at 250 V for 30 min. Protein concentration was determined by measuring the absorbance at 280 nm on a NanoDrop 2000 Spectrophotometer instrument (Thermo Fisher Scientific).

***In Vitro* Disassembly/Reassembly of Encapsulins.** To characterize the *in vitro* disassembly of encapsulins, the presence of a denaturing agent (GuHCl), changes in pH, and thermally induced disassembly methods were used. GuHCl was added to the encapsulin sample to final concentrations between 1 and 7 M. For compatibility and practicality with small volumes, in pH-induced disassembly experiments, 50 mM HEPES buffer solutions with varying pH values (pH 3−13) were prepared via dropwise adjustment with HCl/NaOH, with pH confirmed using pH indicator strips. Once under their respective conditions, encapsulin samples were incubated for 1 h at room temperature and the same sample was subject to all subsequent analysis methods. For thermally induced disassembly, the encapsulin sample was subjected to a temperature ramp from 20−90 °C at a rate of 2 °C/min. In all disassembly methods, the final encapsulin concentration was 5 μM and dithiothreitol (DTT) was added to the encapsulin sample to a final concentration of 1 mM. In GuHCl- and thermally induced disassembly experiments, the desired final volumes were reached by the addition of 50 mM HEPES pH 7.4. For stability experiments, 5 μM of encapsulins was incubated for 1 h at room temperature under reducing (10 mM DTT), oxidizing (10 mM H_2O_2), and high-ionic strength (1 M NaCl) conditions.

The subsequent reassembly of encapsulins was initiated by returning the same sample to original conditions. Briefly, the samples were dialyzed against 50 mM HEPES buffer pH 7.4 and 1 mM DTT at room temperature overnight using a 3.5K MWCO SnakeSkin dialysis tubing (Thermo Fisher Scientific). To measure the reassembly rate, samples were removed from dialysis every 15 min for 75 min and centrifuged for 5 min at 10,000*g* to remove any aggregated proteins.

ITF Spectroscopy. ITF spectroscopy measurements of encapsulins in their varying states of assembly were performed with an FP-8500 spectrofluorometer (JASCO) using a 3 mm pathlength microvolume quartz cuvette. Samples (60 μL) were prepared in triplicate with a final encapsulin concentration of 5 μM. Samples were excited at 290 nm, and emission spectra were collected from 300 to 450 nm. The measurement parameters were as follows: excitation and emission bandwidths of 5 nm, a response of 0.2 s, medium sensitivity, a data interval of 0.1 nm, a scan speed of 100 nm/min, and 4 measurement accumulations were averaged. To investigate the effect of temperature on the different encapsulins, spectra were collected from 20 to 90 °C with a temperature ramp of 2 °C/min. The obtained spectra were further processed by buffer spectra subtraction using Spectra Manager software (JASCO), and the ratio between the fluorescence intensity at 360 and 330 nm (360/330) was calculated and plotted in Microsoft Excel. NFI was achieved by making the maximum emission wavelength (nm) = 1.

Transmission Electron Microscopy. To visualize the morphology, size, and state of encapsulin assembly, TEM was performed using a Philips CM10 microscope (100 kV accelerating voltage). Briefly, encapsulin samples (0.2 mg/mL) were adsorbed onto Pioloform-coated 200 mesh copper grids (ProSciTech) for 2 min. Prior to imaging, samples were negatively stained for 1 h using uranyl acetate replacement (UAR-EMS, Electron Microscopy Sciences), washed with ultrapure water, and allowed to dry for at least 15 min.

Dynamic Light Scattering. To measure the diameter of encapsulins, DLS was performed with a Malvern Zetasizer ZSP instrument equipped with a 633 nm laser. Samples with a final encapsulin concentration of 5 μM were prepared as described above. Three measurements were performed at 25 °C using a plastic microcuvette (ZEN0040, Malvern), with 173° backscatter and automatic attenuator selection. Data analysis was performed in Zetasizer Nano software. All DLS sizes reported, herein, are size by number values calculated using distribution analysis. A 1 cm quartz cuvette was used for temperature ramp experiments. Heat maps were made using GraphPad Prism 9.

Atomic Force Microscopy. Images and force curve measurements were obtained using a Cypher ES Atomic Force Microscope (Oxford Instrument, Asylum Research, Santa Barbara, CA, USA) at room temperature (25 °C). Protocols were adapted from Collett et al.[52,53] For imaging, the instrument was operated in amplitude-modulated AFM (AM-AFM), while force measurements were obtained in the contact mode. Biolever BL-AC40TS cantilevers (Oxford Instruments, Asylum Research, Santa Barbara, CA, USA, nominal spring constant k_c = 0.09 N/m) were used for all measurements. All experiments were completed within a droplet of 50 mM HEPES buffer 7.4 (∼100 μL) with a concentration of ∼100 ng of encapsulins deposited onto the freshly cleaved muscovite surface (the supporting substrate). Prior to experimentation, each cantilever was calibrated via the thermal spectrum method and the lever sensitivity was determined using force

https://doi.org/10.1021/acsomega.1c05472
ACS Omega 2022, 7, 823−836

spectroscopy. Processing of AFM data involved using a combination of the Asylum Research software, custom MATLAB codes, and the Gwyddion software package.[54]

Determining Elasticity of Intact Encapsulins. Force versus distance curves (FD curves) were obtained from the central region of encapsulins. Following image location, FD curves were first obtained on an area of bare mica next to the nanocage to ensure that linear (nonelastic) FD curves were observed, which provided a reference for determining the elasticity of the particles. The spring constant (k_c) of the cantilever was determined for each cantilever used as described above (values in the range of 0.05−0.1 N/m were obtained for all cantilevers). The tip was then directed to the central region of the particle to obtain accurate indentation data. Upward of 50 FD curves were recorded across several particles for each sample.

The tip−sample contact point between the AFM cantilever and the encapsulin was performed independently for each FD curve analyzed using methods previously described.[55] Specifically, the contact point between the AFM cantilever tip and the encapsulin is defined as the point at which the cantilever first makes physical contact with the surface adsorbed particle. Following this point, the cantilever bends in response to interactions with the encapsulin, while the nanocage itself is indented. In a raw FD curve [z-displacement (Z) versus cantilever deflection (d)], this point of first contact is mathematically defined as Z_0 and d_0, respectively. This is observed in the AFM force curve as an increase in force (y-axis), above the zeroed baseline, as a function of distance (x-axis prior to zeroing the indentation).

The indentation (δ) is then calculated via

$$\delta = (z - z_0) - (d - d_0) \quad (1)$$

and transformed into indentation versus force curves using Hooke's law

$$F = K_c \times d \quad (2)$$

The elastic response of the samples is then fit to the Hertz/Sneddon eq 3 to obtain Young's elastic modulus (E) for each of the fitted curves. Using custom MATLAB scripts, curves were fitted to the equations

$$F_{cone} = \frac{2}{\pi} \tan \alpha E^* \delta^2 \quad (3)$$

and

$$E^* = \frac{E}{1 - \nu^2} \quad (4)$$

where F is the loading force, δ is the indentation depth, α is the cone opening angle, E^* is the apparent elastic modulus, and ν is the Poisson ratio. A cone tip angle of 34.4° and a Poisson ratio of 0.5 were used for processing all force curves. All elasticity values were obtained from curves fitted with an R^2 value of 0.9 or above. Data falling below this quality were rejected for further analysis.

■ ASSOCIATED CONTENT

Supporting Information

The Supporting Information is available free of charge at https://pubs.acs.org/doi/10.1021/acsomega.1c05472.

List of genetic constructs, examples of purification chromatographs, gel images of purified encapsulins, molecular graphics of Trp residue positions within encapsulin subunits, gel images of disassembled/reassembled encapsulins, stability study of encapsulins under REDOX and ionic conditions, AFM elasticity histograms, and DLS measurements (PDF)

■ AUTHOR INFORMATION

Corresponding Author

Andrew Care − *School of Life Sciences, University of Technology Sydney, Ultimo, New South Wales 2007, Australia; ARC Centre of Excellence for Nanoscale BioPhotonics and ARC Centre of Excellence in Synthetic Biology, Macquarie University, Macquarie Park, New South Wales 2109, Australia;* orcid.org/0000-0002-0035-7961; Email: andrew.care@uts.edu.au

Authors

India Boyton − *School of Life Sciences, University of Technology Sydney, Ultimo, New South Wales 2007, Australia; ARC Centre of Excellence for Nanoscale BioPhotonics, Macquarie University, Macquarie Park, New South Wales 2109, Australia*

Sophia C. Goodchild − *Department of Molecular Sciences, Macquarie University, Macquarie Park, New South Wales 2109, Australia*

Dennis Diaz − *Department of Molecular Sciences, Macquarie University, Macquarie Park, New South Wales 2109, Australia*

Aaron Elbourne − *School of Science, College of Science, Engineering and Health, RMIT University, Melbourne, Victoria 3000, Australia;* orcid.org/0000-0002-4472-4372

Lyndsey E. Collins-Praino − *Adelaide Medical School, The University of Adelaide, Adelaide, South Australia 5005, Australia; ARC Centre of Excellence for Nanoscale BioPhotonics, Macquarie University, Macquarie Park, New South Wales 2109, Australia*

Complete contact information is available at: https://pubs.acs.org/10.1021/acsomega.1c05472

Author Contributions

I.B. co-designed the research, generated all nanocage constructs, conducted all disassembly/reassembly characterization work, performed data analysis, and wrote the manuscript. S.C.G assisted in experimental design and data interpretation and wrote the manuscript. D.D. assisted in protein production and purification, TEM imaging, and protein modelling and revised the manuscript. A.E performed AFM experiments and data analysis. L.E.C.-P supervised the project and revised the manuscript. A.C. conceptualized and co-designed the study, supervised the project, and wrote the manuscript.

Notes

The authors declare no competing financial interest.

■ ACKNOWLEDGMENTS

I.B. was supported by a Dementia Australia Research Foundation PhD scholarship. A.C. was supported by a UTS Chancellor's Postdoctoral Research Fellowship and the Cancer Australia Priority-driven Collaborative Cancer Research Scheme (Project 1182082). This work was also supported by grants to A.C. and L.E.C.-P by the Dementia Australia

https://doi.org/10.1021/acsomega.1c05472
ACS Omega 2022, 7, 823−836

Research Foundation, the National Foundation for Medical Research and Innovation, the Brain Foundation, and the NeuroSurgical Research Foundation. Figures were created in BioRender.

REFERENCES

(1) Diaz, D.; Care, A.; Sunna, A. Bioengineering Strategies for Protein-Based Nanoparticles. *Genes* **2018**, *9*, 370.
(2) Sandra, F.; Khaliq, N. U.; Sunna, A.; Care, A. Developing protein-based nanoparticles as versatile delivery systems for cancer therapy and imaging. *Nanomaterials* **2019**, *9*, 1329.
(3) Jones, J. A.; Giessen, T. W. Advances in encapsulin nanocompartment biology and engineering. *Biotechnol. Bioeng.* **2021**, *118*, 491−505.
(4) Gabashvili, A. N.; Chmelyuk, N. S.; Efremova, M. V.; Malinovskaya, J. A.; Semkina, A. S.; Abakumov, M. A. Encapsulins—Bacterial protein nanocompartments: Structure, properties, and application. *Biomolecules* **2020**, *10*, 966.
(5) Sutter, M.; Boehringer, D.; Gutmann, S.; Günther, S.; Prangishvili, D.; Loessner, M. J.; Stetter, K. O.; Weber-Ban, E.; Ban, N. Structural basis of enzyme encapsulation into a bacterial nanocompartment. *Nat. Struct. Mol. Biol.* **2008**, *15*, 939.
(6) Giessen, T. W.; Orlando, B. J.; Verdegaal, A. A.; Chambers, M. G.; Gardener, J.; Bell, D. C.; Birrane, G.; Liao, M.; Silver, P. A. Large protein organelles form a new iron sequestration system with high storage capacity. *eLife* **2019**, *8*, No. e46070.
(7) Sigmund, F.; Pettinger, S.; Kube, M.; Schneider, F.; Schifferer, M.; Schneider, S.; Efremova, M. V.; Pujol-Martí, J.; Aichler, M.; Walch, A.; Misgeld, T.; Dietz, H.; Westmeyer, G. G. Iron-sequestering nanocompartments as multiplexed Electron Microscopy gene reporters. *ACS Nano* **2019**, *13*, 8114−8123.
(8) McHugh, C. A.; Fontana, J.; Nemecek, D.; Cheng, N.; Aksyuk, A. A.; Heymann, J. B.; Winkler, D. C.; Lam, A. S.; Wall, J. S.; Steven, A. C.; Hoiczyk, E. A virus capsid-like nanocompartment that stores iron and protects bacteria from oxidative stress. *EMBO J.* **2014**, *33*, 1896−1911.
(9) Giessen, T. W.; Silver, P. A. Widespread distribution of encapsulin nanocompartments reveals functional diversity. *Nat. Microbiol.* **2017**, *2*, 17029.
(10) Contreras, H.; Joens, M. S.; McMath, L. M.; Le, V. P.; Tullius, M. V.; Kimmey, J. M.; Bionghi, N.; Horwitz, M. A.; Fitzpatrick, J. A. J.; Goulding, C. W. Characterization of a Mycobacterium tuberculosis nanocompartment and its potential cargo proteins. *J. Biol. Chem.* **2014**, *289*, 18279−18289.
(11) He, D.; Hughes, S.; Vanden-Hehir, S.; Georgiev, A.; Altenbach, K.; Tarrant, E.; Mackay, C. L.; Waldron, K. J.; Clarke, D. J.; Marles-Wright, J. Structural characterization of encapsulated ferritin provides insight into iron storage in bacterial nanocompartments. *eLife* **2016**, *5*, No. e18972.
(12) Nichols, R. J.; LaFrance, B.; Phillips, N. R.; Radford, D. R.; Oltrogge, L. M.; Valentin-Alvarado, L. E.; Bischoff, A. J.; Nogales, E.; Savage, D. F. Discovery and characterization of a novel family of prokaryotic nanocompartments involved in sulfur metabolism. *eLife* **2021**, *10*, No. e59288.
(13) Diaz, D.; Vidal, X.; Sunna, A.; Care, A. Bioengineering a Light-Responsive Encapsulin Nanoreactor: A Potential Tool for In Vitro Photodynamic Therapy. *ACS Appl. Mater. Interfaces* **2021**, *13*, 7977−7986.
(14) McManus, J. J.; Charbonneau, P.; Zaccarelli, E.; Asherie, N. The physics of protein self-assembly. *Curr. Opin. Colloid Interface Sci.* **2016**, *22*, 73−79.
(15) Zhang, Y.; Orner, B. P. Self-assembly in the ferritin nano-cage protein superfamily. *Int. J. Mol. Sci.* **2011**, *12*, 5406−5421.
(16) Gerl, M.; Jaenicke, R. Mechanism of the self-assembly of apoferritin from horse spleen. *Eur. Biophys. J.* **1987**, *15*, 103−109.
(17) Gerl, M.; Jaenicke, R.; Smith, J. M. A.; Harrison, P. M. Self-assembly of apoferritin from horse spleen after reversible chemical modification with 2, 3-dimethylmaleic anhydride. *Biochemistry* **1988**, *27*, 4089−4096.
(18) Crichton, R. R.; Bryce, C. F. A. Subunit interactions in horse spleen apoferritin. Dissociation by extremes of pH. *Biochem. J.* **1973**, *133*, 289−299.
(19) Kim, M.; Rho, Y.; Jin, K. S.; Ahn, B.; Jung, S.; Kim, H.; Ree, M. pH-dependent structures of ferritin and apoferritin in solution: disassembly and reassembly. *Biomacromolecules* **2011**, *12*, 1629−1640.
(20) Mohanty, A.; K, M.; Jena, S. S.; Behera, R. K. Kinetics of Ferritin Self-Assembly by Laser Light Scattering: Impact of Subunit Concentration, pH, and Ionic Strength. *Biomacromolecules* **2021**, *22*, 1389−1398.
(21) Chen, H.; Zhang, S.; Xu, C.; Zhao, G. Engineering protein interfaces yields ferritin disassembly and reassembly under benign experimental conditions. *Chem. Commun.* **2016**, *52*, 7402−7405.
(22) Cassidy-Amstutz, C.; Oltrogge, L.; Going, C. C.; Lee, A.; Teng, P.; Quintanilla, D.; East-Seletsky, A.; Williams, E. R.; Savage, D. F. Identification of a minimal peptide tag for in vivo and in vitro loading of encapsulin. *Biochemistry* **2016**, *55*, 3461−3468.
(23) Künzle, M.; Mangler, J.; Lach, M.; Beck, T. Peptide-directed encapsulation of inorganic nanoparticles into protein containers. *Nanoscale* **2018**, *10*, 22917−22926.
(24) Jones, J. A.; Cristie-David, A. S.; Andreas, M. P.; Giessen, T. W. Triggered reversible disassembly of an engineered protein nanocage. *Angew. Chem., Int. Ed.* **2021**, *60*, 25034−25041.
(25) Lakowicz, J. R. *Principles of Fluorescence Spectroscopy*, 3rd ed.; Springer: New York, 2006.
(26) Sonotaki, S.; Noguchi, K.; Yohda, M.; Murakami, Y. A zeolite as a tool for successful refolding of PEGylated proteins and their reassembly with tertiary structures. *Biotechnol. Prog.* **2019**, *35*, No. e2853.
(27) Bhattacharjee, C.; Das, K. P. Thermal unfolding and refolding of β-lactoglobulin: An intrinsic and extrinsic fluorescence study. *Eur. J. Biochem.* **2000**, *267*, 3957−3964.
(28) Reshetnyak, Y. K.; Burstein, E. A. Decomposition of protein tryptophan fluorescence spectra into log-normal components. II. The statistical proof of discreteness of tryptophan classes in proteins. *Biophys. J.* **2001**, *81*, 1710−1734.
(29) Chaudhary, A. P.; Vispute, N. H.; Shukla, V. K.; Ahmad, B. A comparative study of fibrillation kinetics of two homologous proteins under identical solution condition. *Biochimie* **2017**, *132*, 75−84.
(30) Pettersen, E. F.; Goddard, T. D.; Huang, C. C.; Meng, E. C.; Couch, G. S.; Croll, T. I.; Morris, J. H.; Ferrin, T. E. UCSF ChimeraX: Structure visualization for researchers, educators, and developers. *Protein Sci.* **2021**, *30*, 70−82.
(31) Zhou, B.; Wan, J.; Wang, J.; Cao, X. Effect of chaotropes in reverse micellar extraction of kallikrein. *Process Biochem.* **2012**, *47*, 229−233.
(32) Snijder, J.; Kononova, O.; Barbu, I. M.; Uetrecht, C.; Rurup, W. F.; Burnley, R. J.; Koay, M. S. T.; Cornelissen, J. J. L. M.; Roos, W. H.; Barsegov, V.; Wuite, G. J. L.; Heck, A. J. R. Assembly and mechanical properties of the cargo-free and cargo-loaded bacterial nanocompartment encapsulin. *Biomacromolecules* **2016**, *17*, 2522−2529.
(33) Martsev, S. P.; Vlasov, A. P.; Arosio, P. Distinct stability of recombinant L and H subunits of human ferritin: calorimetric and ANS binding studies. *Protein Eng.* **1998**, *11*, 377−381.
(34) Liang, M.; Fan, K.; Zhou, M.; Duan, D.; Zheng, J.; Yang, D.; Feng, J.; Yan, X. H-ferritin−nanocaged doxorubicin nanoparticles specifically target and kill tumors with a single-dose injection. *Proc. Natl. Acad. Sci. U.S.A.* **2014**, *111*, 14900−14905.
(35) Yang, R.; Liu, Y.; Blanchard, C.; Zhou, Z. Channel directed rutin nano-encapsulation in phytoferritin induced by guanidine hydrochloride. *Food Chem.* **2018**, *240*, 935−939.
(36) Sharma, J.; Uchida, M.; Miettinen, H. M.; Douglas, T. Modular interior loading and exterior decoration of a virus-like particle. *Nanoscale* **2017**, *9*, 10420−10430.
(37) Gasteiger, E.; Gattiker, A.; Hoogland, C.; Ivanyi, I.; Appel, R. D.; Bairoch, A. ExPASy: the proteomics server for in-depth protein knowledge and analysis. *Nucleic Acids Res.* **2003**, *31*, 3784−3788.

https://doi.org/10.1021/acsomega.1c05472
ACS Omega 2022, 7, 823−836

(38) Zhou, H.-X.; Pang, X. Electrostatic interactions in protein structure, folding, binding, and condensation. *Chem. Rev.* **2018**, *118*, 1691−1741.
(39) Vos, M.; Velicer, G. J. Genetic population structure of the soil bacterium Myxococcus xanthus at the centimeter scale. *Appl. Environ. Microbiol.* **2006**, *72*, 3615−3625.
(40) Asor, R.; Khaykelson, D.; Ben-nun-Shaul, O.; Oppenheim, A.; Raviv, U. Effect of calcium ions and disulfide bonds on swelling of virus particles. *ACS Omega* **2019**, *4*, 58−64.
(41) Altenburg, W. J.; Rollins, N.; Silver, P. A.; Giessen, T. W. Exploring targeting peptide-shell interactions in encapsulin nanocompartments. *Sci. Rep.* **2021**, *11*, 4951.
(42) Hellmann, N.; Schneider, D. Hands On: Using Tryptophan Fluorescence Spectroscopy to Study Protein Structure. *Methods Mol. Biol.* **2019**, *1958*, 379−401.
(43) Kelly, S. M.; Jess, T. J.; Price, N. C. How to study proteins by circular dichroism. *Biochim. Biophys. Acta, Proteins Proteomics* **2005**, *1751*, 119−139.
(44) Faulkner, M.; Rodriguez-Ramos, J.; Dykes, G. F.; Owen, S. V.; Casella, S.; Simpson, D. M.; Beynon, R. J.; Liu, L.-N. Direct characterization of the native structure and mechanics of cyanobacterial carboxysomes. *Nanoscale* **2017**, *9*, 10662−10673.
(45) Heinze, K.; Sasaki, E.; King, N. P.; Baker, D.; Hilvert, D.; Wuite, G. J. L.; Roos, W. H. Protein nanocontainers from nonviral origin: testing the mechanics of artificial and natural protein cages by AFM. *J. Phys. Chem. B* **2016**, *120*, 5945−5952.
(46) de Pablo, P. J. The application of atomic force microscopy for viruses and protein shells: imaging and spectroscopy. *Adv. Virus Res.* **2019**, *105*, 161−187.
(47) Sutter, M.; Faulkner, M.; Aussignargues, C.; Paasch, B. C.; Barrett, S.; Kerfeld, C. A.; Liu, L.-N. Visualization of bacterial microcompartment facet assembly using high-speed atomic force microscopy. *Nano Lett.* **2016**, *16*, 1590−1595.
(48) Stühn, L.; Auernhammer, J.; Dietz, C. pH-depended protein shell dis-and reassembly of ferritin nanoparticles revealed by atomic force microscopy. *Sci. Rep.* **2019**, *9*, 17755.
(49) Schmitt, N. D.; Berger, J. M.; Conway, J. B.; Agar, J. N. Increasing Top-Down Mass Spectrometry Sequence Coverage by an Order of Magnitude through Optimized Internal Fragment Generation and Assignment. *Anal. Chem.* **2021**, *93* (16), 6355−6362.
(50) Le Vay, K.; Carter, B. M.; Watkins, D. W.; Dora Tang, T.-Y.; Ting, V. P.; Cölfen, H.; Rambo, R. P.; Smith, A. J.; Ross Anderson, J. L.; Perriman, A. W. Controlling protein nanocage assembly with hydrostatic pressure. *J. Am. Chem. Soc.* **2020**, *142*, 20640−20650.
(51) Sasaki, E.; Böhringer, D.; Van de Waterbeemd, M.; Leibundgut, M.; Zschoche, R.; Heck, A. J.; Ban, N.; Hilvert, D. Structure and assembly of scalable porous protein cages. *Nat. Commun.* **2017**, *8*, 14663.
(52) Collett, S.; Torresi, J.; Earnest-Silveira, L.; Christiansen, D.; Elbourne, A.; Ramsland, P. A. Probing and pressing surfaces of hepatitis C virus-like particles. *J. Colloid Interface Sci.* **2019**, *545*, 259−268.
(53) Collett, S.; Torresi, J.; Silveira, L. E.; Truong, V. K.; Christiansen, D.; Tran, B. M.; Vincan, E.; Ramsland, P. A.; Elbourne, A. Investigating virus−host cell interactions: Comparative binding forces between hepatitis C virus-like particles and host cell receptors in 2D and 3D cell culture models. *J. Colloid Interface Sci.* **2021**, *592*, 371−384.
(54) Nečas, D.; Klapetek, P. Gwyddion: an open-source software for SPM data analysis. *Open Phys.* **2012**, *10*, 181−188.
(55) Touhami, A.; Nysten, B.; Dufrêne, Y. F. Nanoscale Mapping of the Elasticity of Microbial Cells by Atomic Force Microscopy. *Langmuir* **2003**, *19*, 4539−4543.

https://doi.org/10.1021/acsomega.1c05472
ACS Omega 2022, 7, 823−836